Applied Surface Science

Lignin-derived carbon quantum dots-decorated Bi7O9I3 nanosheets with enhanced photocatalytic performance: Synergism of electron transfer acceleration and molecular oxygen activation

--Manuscript Draft--

Manuscript Number:	APSUSC-D-22-10367
Article Type:	Full Length Article
Keywords:	CQDs/Bi7O9I3 composite; photocatalytic degradation; tetracycline hydrochloride; photocatalytic mechanism
Corresponding Author:	Dekui Shen Southeast University Nanjing, CHINA
First Author:	Lingli Zhu
Order of Authors:	Lingli Zhu
	Dekui Shen
	Kai Hong Luo
Abstract:	The design and development of high-efficient photocatalyst are confined by the limited light-harvesting capacity and rapid electron-hole recombination. The Bi7O9I3 nanosheets decorated by lignin-derived carbon quantum dots (CQDs) were prepared through a simple hydrothermal process, which was employed for the photocatalytic degradation of tetracycline hydrochloride (TC). The prepared CQDs/Bi7O9I3 composite with the CQDs content of 3% showed the optimal photocatalytic degradation efficiency of 100% in 45 min under 300 W Xe lamp irradiation. The corresponding degradation rate was 0.08133 min-1 , which was 4.74 times higher than that of pure Bi7O9I3 . The superoxide (•O2-) and hole (h+) radicals were identified as the key reactive species for TC degradation through the photocatalytic mechanism exploration. The photocatalytic activity of CQDs/Bi7O9I3 with 3% CQDs content could maintain above 80% after five recycles of TC degradation reaction, signifying its outstanding stability and reusability. The superior photocatalytic performance of CQDs/Bi7O9I3 is explained by the enhanced sunlight harvesting ability, the accelerated electron transfer, and the formation of reactive species thanks to the incorporation of CQDs. It offers a promising strategy for constructing high-performance and environmentally friendly photocatalysts for contaminant water treatment through the decoration of biomass-derived CQDs.
Suggested Reviewers:	Chunfei Wu Queen's University Belfast c.wu@hull.ac.uk
	Sai Gu University of Surrey sai.gu@surrey.ac.uk
	Kuan Ding Nanjing Forestry University dingk@njfu.edu.cn
	Haiping Yang Huazhong University of Science and Technology yhping2002@163.com

Highlights

- The lignin-derived carbon quantum dots (CQDs) decorated $Bi_7O_9I_3$ nanosheets are prepared through a facile hydrothermal method.

- The effects of different CQDs contents on the photocatalytic performance are researched comparatively.

- The photocatalytic mechanism for TC degradation on CQDs/$Bi_7O_9I_3$ composite is revealed.

Graphic abstract

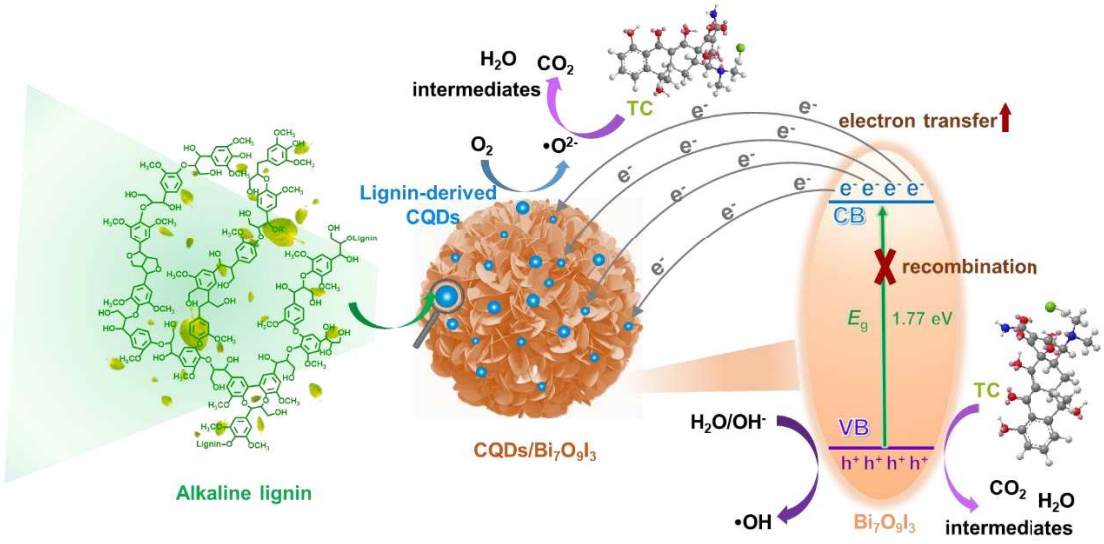

Lignin-derived carbon quantum dots-decorated $Bi_7O_9I_3$ nanosheets with enhanced photocatalytic performance: Synergism of electron transfer acceleration and molecular oxygen activation

Lingli Zhu[a], Dekui Shen[a,*] Kai Hong Luo[b]

[a] Key Laboratory of Energy Thermal Conversion and Control of Ministry of Education, School of Energy and Environment, Southeast University, Nanjing 210096, PR China.

[b] Department of Mechanical Engineering, University College London, London WC1E7JE, U.K.

E-mail address: 101011398@seu.edu.cn (D. Shen)

Abstract: The design and development of high-efficient photocatalyst are confined by the limited light-harvesting capacity and rapid electron-hole recombination. The $Bi_7O_9I_3$ nanosheets decorated by lignin-derived carbon quantum dots (CQDs) were prepared through a simple hydrothermal process, which was employed for the photocatalytic degradation of tetracycline hydrochloride (TC). The prepared CQDs/$Bi_7O_9I_3$ composite with the CQDs content of 3% showed the optimal photocatalytic degradation efficiency of 100% in 45 min under 300 W Xe lamp irradiation. The corresponding degradation rate was 0.08133 min^{-1}, which was 4.74 times higher than that of pure $Bi_7O_9I_3$. The superoxide ($\bullet O^{2-}$) and hole (h^+) radicals were identified as the key reactive species for TC degradation through the photocatalytic mechanism exploration. The photocatalytic activity of CQDs/$Bi_7O_9I_3$ with 3% CQDs content could maintain above 80% after five recycles of TC degradation reaction, signifying its outstanding stability and reusability. The superior photocatalytic performance of CQDs/$Bi_7O_9I_3$ is explained by the enhanced sunlight harvesting ability, the accelerated electron transfer, and the formation of reactive species thanks to the incorporation of CQDs. It offers a promising strategy for constructing high-performance and environmentally friendly photocatalysts for contaminant water treatment through the decoration of biomass-derived CQDs.

Keywords: CQDs/$Bi_7O_9I_3$ composite, photocatalytic degradation, tetracycline hydrochloride, photocatalytic mechanism

1. Introduction

The increasing global environmental pollution in water caused by the excessive use of antibiotics adds serious risk to the ecological surrounding and human health [1, 2]. The elimination of antibiotics from the water system becomes an urgent issue. As compared to the conventional treatment plans (ion exchange and adsorption), photocatalysis is considered to be a clean technology for the removal of antibiotics due to its sustainability, cost-effectiveness and environmental friendliness [3, 4]. A variety of metal oxides have made certain advances in the photocatalytic degradation of antibiotics, for instance, TiO_2, ZnO, Fe_2O_3, WO_3, etc [5-7]. However, these metal oxides possess a wide band gap, a weak reduction ability range as well as a narrow visible light response [8]. Their activity presents a significant limitation under visible light, while visible light accounts for ~50% of solar energy [9]. The development of efficient photocatalysts to fully utilize solar energy is the foremost priority.

The energy bandwidth of metal oxides can be narrowed by forming new valence band energy levels or electron donor energy levels between the O_{2p} orbitals and other elements, thus enhancing the photocatalytic performance. Currently, bismuth halide oxide BiOX (X = F, Cl, Br, I) exhibits outstanding degradation ability of organic pollutants and has drawn extensive interest for its unique layered and electronic structure, and excellent visible light absorption ability [10, 11]. Nevertheless, the rapid recombination of photo-generated electro-hole pairs and insufficient sunlight absorption in the single-phase Bi-based materials are the key factors to limit photocatalytic performance [12]. Carbon quantum dots (CQDs) as an emerging zero-dimensional (0D) carbon nanomaterial with a size less than 10 nm, have aroused increasing concern in photocatalytic applications [13]. It possesses an amorphous nanocrystal core composed mainly of sp^2 conjugated structure and is enriched with oxygen in the form of hydroxyl and carboxyl groups, which contributes to the superior electronic storage capacity of CQDs [14]. CQDs may be applied as a co-catalyst to construct surface separation centers for electron-holes, thus inhibiting their recombination [15, 16]. Newly, CQDs have been coupled with Bi-based photocatalysts such as CQDs/BiOCl [17], CQDs/BiOBr [11, 18], and CQDs/$BiOIO_3$ [10] to enhance their photocatalytic activity, but the related studies are still limited. It is determined that the band gap of BiOX decreases in order with F, Cl, Br, and I. Compared with BiOCl and BiOBr, $BiOIO_3$ shows greater visible light absorption ability and narrower band gap. Moreover, nitrogen doping is effective in inducing charge delocalization, reducing the work function and promoting the electron transfer capability of CQDs [16, 18]. The superior photocatalytic activity of different heteroatoms doped CQDs decorated Bi-based photocatalysts is expected and needs to be further investigated.

Herein, the $Bi_7O_9I_3$ nanosheets decorated by lignin-derived CQDs were synthesized via a simple hydrothermal process. The morphologies, structures and optical-electronic characteristics of CQDs/$Bi_7O_9I_3$ composites were investigated in detail. The photocatalytic activity of CQDs/$Bi_7O_9I_3$ composites was estimated through photodegradation of tetracycline hydrochloride (TC). The photocatalytic mechanism was revealed by free radical trapping experiments and electron paramagnetic resonance (EPR) analysis.

2. Experimental section

2.1 Chemicals and materials

Alkali lignin (AL) with 4% sulfur content was provided by Sigma Aldrich in Shanghai, China. 3-Aminophenylboronic acid hemisulfate, bismuth nitrate hydrate ($Bi(NO_3)_3·5H_2O$), potassium iodide (KI), ethylene glycol (EG), TC, isopropanol (IPA), 1, 4-benzoquinone (1, 4-BQ), and ethylene diamine tetraacetic acid disodium salt dihydrate (EDTA-2Na) were obtained from Aladdin in Shanghai, China. All chemical reagents were of analytical grade and were used without further purification. The dialysis bag (3000 Da) was supplied by Viskase in the USA. The PTFE microporous filter membranes with pore diameters of 0.8 and 0.22 μm were purchased from Jinteng in Tianjin, China. Deionized water (DI, 18 MΩ) was used throughout the experiment.

2.2 Synthesis of photocatalysts

2.2.1 Synthesis of lignin-derived CQDs

The lignin-derived CQDs were prepared by a two-step route by the previously reported method [19]. Briefly, 0.8 g of 3-Aminophenylboronic acid hemisulfate acid and 0.8 g of AL were solubilized in 240 mL of DI water with continuous magnetic stirring at 90 °C for 1 h. Then, the filtered liquid was moved into a 300 mL Teflon-lined stainless autoclave and maintained at 200 °C for 12 h. Subsequently, the yellow-brown solution was filtered and purified in a dialysis bag for 48 h. The light yellow CQDs powder was finally obtained after vacuum freeze-dried for 48 h.

2.2.2 Synthesis of $Bi_7O_9I_3$ and CQDs/$Bi_7O_9I_3$ composites

The CQDs decorated $Bi_7O_9I_3$ composites were fabricated via a hydrothermal process as presented in Scheme 1. Typically, 4.368 g of $Bi(NO_3)_3·5H_2O$ was dispersed into 120 mL EG

with sonicating for 30 min to get solution A. 1.494 g of KI and a designed amount of CQDs powder were mixed into 120 mL EG with sonicating for 30 min to get solution B. Then, solution A was manually added to solution B and stirred continuously for 2 h. Afterwards, the mixed solution was moved into a 300 mL Teflon-lined autoclave and kept at 160 ◦C for 24 h. The resulting solution was centrifugalized at high speed and cleaned four times with DI water. The CQDs/$Bi_7O_9I_3$ powers were obtained through drying at 70 °C for 12 h. For comparison, the mass ratio of CQDs to $Bi_7O_9I_3$ was controlled at 1 wt%, 3 wt% and 5 wt%, which were denoted as CQDs/$Bi_7O_9I_3$-1, CQDs/$Bi_7O_9I_3$-3, and CQDs/$Bi_7O_9I_3$-5, respectively. The pure $Bi_7O_9I_3$ was obtained using the above similar procedure in the absence of CQDs.

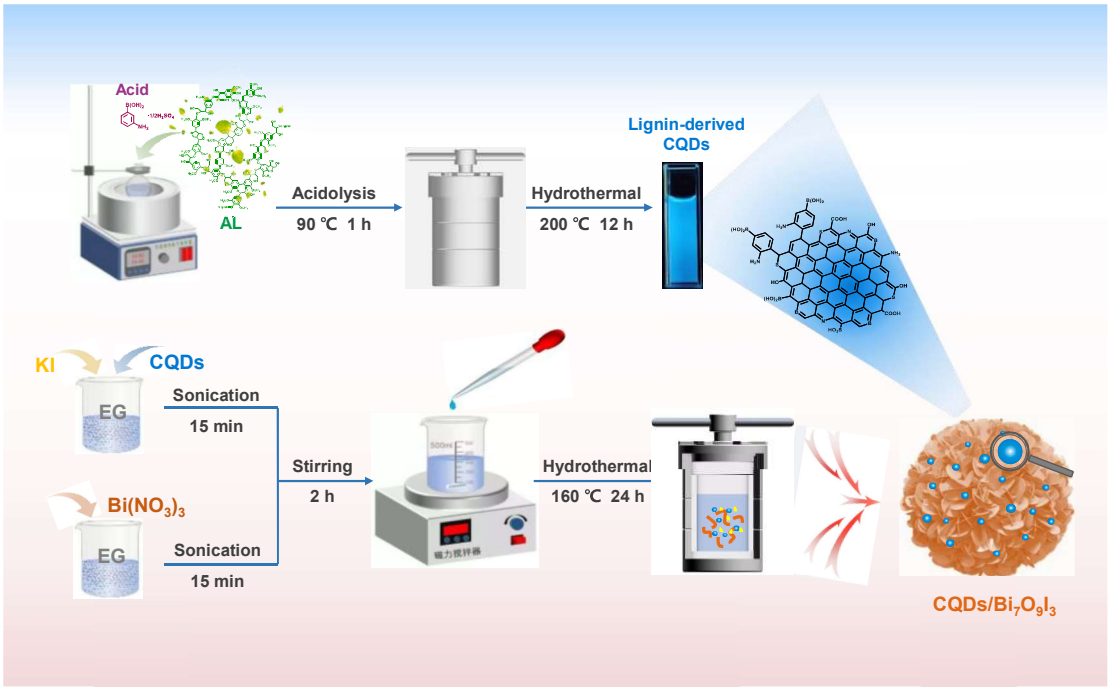

Scheme 1. Diagram of the synthesis process of CQDs/$Bi_7O_9I_3$ composites.

2.3 Characterization

The X-ray diffraction (XRD, Bruker D2 PHASER) patterns were detected via the X-ray powder diffraction instrument with Cu Ka radiation. The morphology features were analyzed by scanning electron microscope (SEM, ZEISS Sigma 300), and the transmission electron microscope, higher transmission electron microscope (TEM, HR-TEM, FEI Talos F200s) with the energy dispersive spectrometer (EDS, FEI Super-X EDS Detector). The surface chemical structure was implemented on an X-ray photoelectron spectroscopy (XPS, Thermo ESCALAB 250XI). The surface structure was recorded on a Fourier transform infrared spectrometer (FT-IR, Thermo Scientific Nicolet iS20). The light absorption capacity (200~800 nm) was analyzed by a UV–Vis diffuse reflectance spectrophotometer (UV–Vis DRS, Shimadzu UV-3600i Plus).

The photoluminescence spectra were performed on a fluorescence spectrophotometer (PL, Agilent Cary Eclipse). The electron paramagnetic resonance spectra were measured on an electron paramagnetic resonance spectrometer (EPR, Bruker EMXplus-6/1) with 5, 5-dimethyl-1-pyrroline N-oxide (DMPO, 50 μL).

2.4 Photocatalytic degradation of TC

The photocatalytic activity of the photocatalysts was assessed through TC degradation under simulated sunlight irradiation. In brief, 50 mg of the photocatalyst was put into TC (20 mg/L, 200 ml) solution and the mixture with continuous stirring for 30 min in the darkness. After that, the photocatalytic reactions were carried out under 300 W Xe lamp irradiation (100 mW/cm^2, Beijing China Education Au-light CEL-PF300-T6). The different reaction solutions were taken out at specific time intervals and filtered through a 0.22 μm microporous filter membrane. The corresponding concentration of TC in the solution was measured by UV-Vis spectrophotometer at an absorption wavelength of 357 nm. The recyclability of CQDs/$Bi_7O_9I_3$ composites was obtained through four successive cycling experiments. The degradation efficiency was calculated by **Eq. 1**:

$$\eta = \frac{C_0 - C}{C_0} \times 100\% = \frac{A_0 - A_t}{A_0} \times 100\% \quad (1)$$

where η indicates the degradation efficiency, C_0 and C represent the initial and instant concentration of TC, respectively.

The trapping experiments were implemented to determine the impacts of reactive species including superoxide radical ($\cdot O_2^-$), holes (h^+), and hydroxyl radical (·OH) on the photocatalytic process of CQDs/$Bi_7O_9I_3$ composites. IPA, 1, 4-BQ, and EDTA-2Na (0.1 mol/L) served as the scavenger for $\cdot O_2^-$, h^+, and ·OH, respectively. The experimental procedures were the same as those in the tests of photocatalytic activity.

2.5 Photoelectrochemical evaluation

The transient photocurrent response (i-t) and electrochemical impedance spectra (EIS) were tested on an electrochemical system (CHI-660E, Shanghai Chenhua) with a three-electrode cell. The saturated Ag/AgCl electrode, Pt wire and 0.5 M Na_2SO_4 were used as reference electrode, counter electrode and electrolyte solution, respectively. The working electrodes were fabricated of FTO glass with the prepared photocatalysts attached to it. Typically, 10 mg of photocatalyst was completely dispersed in 1 mL of ethanol and 30 μL of naphthol. The mucilage was subsequently dripped uniformly onto a 10 x 20 mm FTO.

3. Results and discussion

3.1 Morphology and structural characterization

The crystalline structure of CQDs, pure $Bi_7O_9I_3$, and CQDs/$Bi_7O_9I_3$ composites with the adjustment of CQDs contents of 1%~3% can be validated by XRD. As displayed in **Fig. 1**a, the distinct diffraction peaks at 28.5°, 32.1°, 45.9°, and 55.0° are corresponding to the (102), (110), (200), (1 3 3), and (212) crystal planes of orthorhombic $Bi_7O_9I_3$ (JCPDS 40-0548) [20], respectively. The weak characteristic peak (002) around 26.5° from CQDs/$Bi_7O_9I_3$-1 to CQDs/$Bi_7O_9I_3$-3 slightly strengthens with the increasing content of CQDs [21]. Obviously, $Bi_7O_9I_3$ is the predominant constituent in the composites, and the modification of CQDs might not inhibit the growth of $Bi_7O_9I_3$ crystal. The FTIR spectra of the prepared photocatalysts are shown in **Fig. 1**b. For CQDs, the peaks at 3423, 1719, 1600, 1364, 1106, 759, and 623 cm^{-1} are assigned to stretching vibrations of O-H/N-H, C=O, C=C, C-O, C-N, B-O and C-S bonds, indicating the N, S, and B co-doping of CQDs [19, 22]. The FT-IR spectrum of pure $Bi_7O_9I_3$ has characteristic peaks at 3420, 1593 cm^{-1} corresponding to the O-H, H-O-H bonds of adsorbed H_2O, and 1380, 1066, 881, 507 cm^{-1} of I-O-I, Bi-O, and I-O bonds, respectively [23, 24]. For the CQDs/$Bi_7O_9I_3$ composites, their FT-IR spectra are the combined result of $Bi_7O_9I_3$ along with the low content of CQDs. The intensity of emerging peaks at 1746, 1305, and 765 cm^{-1} of C=O, C-O, and B-O bonds increase gradually as the content of CQDs increases [14]. It can be further concluded that the $Bi_7O_9I_3$ photocatalyst is modified by CQDs successfully.

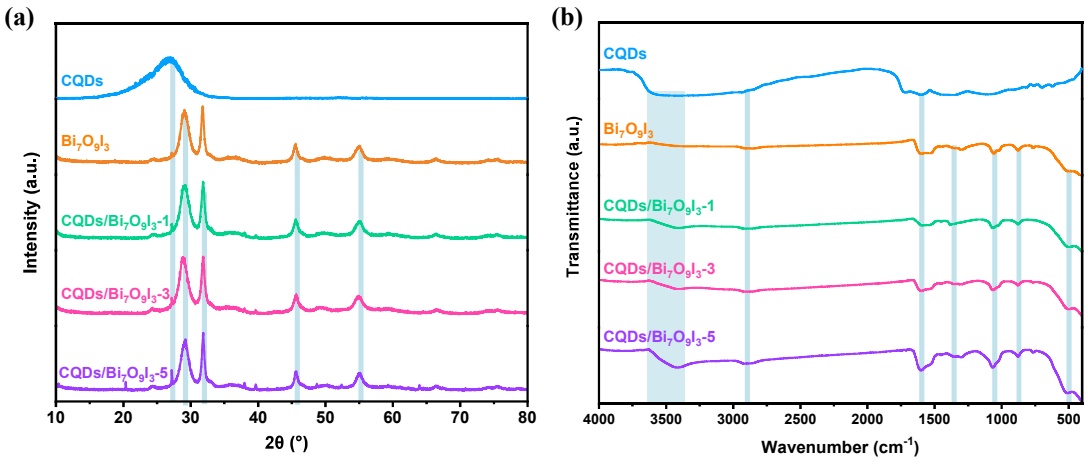

Fig. 1. XRD patterns and FTIR spectra of CQDs, $Bi_7O_9I_3$, and CQDs/$Bi_7O_9I_3$ composites.

The morphology of CQDs, pure $Bi_7O_9I_3$, and CQDs/$Bi_7O_9I_3$ composite can be observed by SEM, TEM and HR-TEM. The TEM and HR-TEM images (**Fig. S1**) show that CQDs are dispersed 0D quasi-spherical nanodots below 10 nm. The SEM images of pure $Bi_7O_9I_3$ in **Fig.**

2a-c present a stacked 3D layered flower-like microstructure with a diameter of ~2 μm. The SEM images of the CQDs decorated $Bi_7O_9I_3$ composite in Fig. 2d-f display a small amount of rough and irregular surfaces grown on the nanoflakes due to the non-uniformity of CQDs. This special morphology facilitates electron transfer and adsorption of contaminants. The TEM and HR-TEM images of the CQDs/$Bi_7O_9I_3$ (Fig. 2g-i) exhibit that the small-sized CQDs are attached to the surface of the nanosheet without changing the size and morphology of the $Bi_7O_9I_3$ main structure. The lattice spacings of 0.31 nm and 0.281 nm are ascribed to the (002) crystal plane of CQDs and (100) crystal plane of $Bi_7O_9I_3$, respectively. The elemental mapping (Fig. 2j-q) shows that CQDs/$Bi_7O_9I_3$ composite contains Bi, I, O, C, N, S, and B, all of which are clearly distributed. Additionally, the EDS analysis (Fig. 2r) shows that the percentages of Bi, I, O, C, N, S, and B are 48.77, 26.05, 24.67, 0.39, 0.13 and less than 0.01%. The SEM and TEM analyses confirm the successful coupling of CQDs with $Bi_7O_9I_3$.

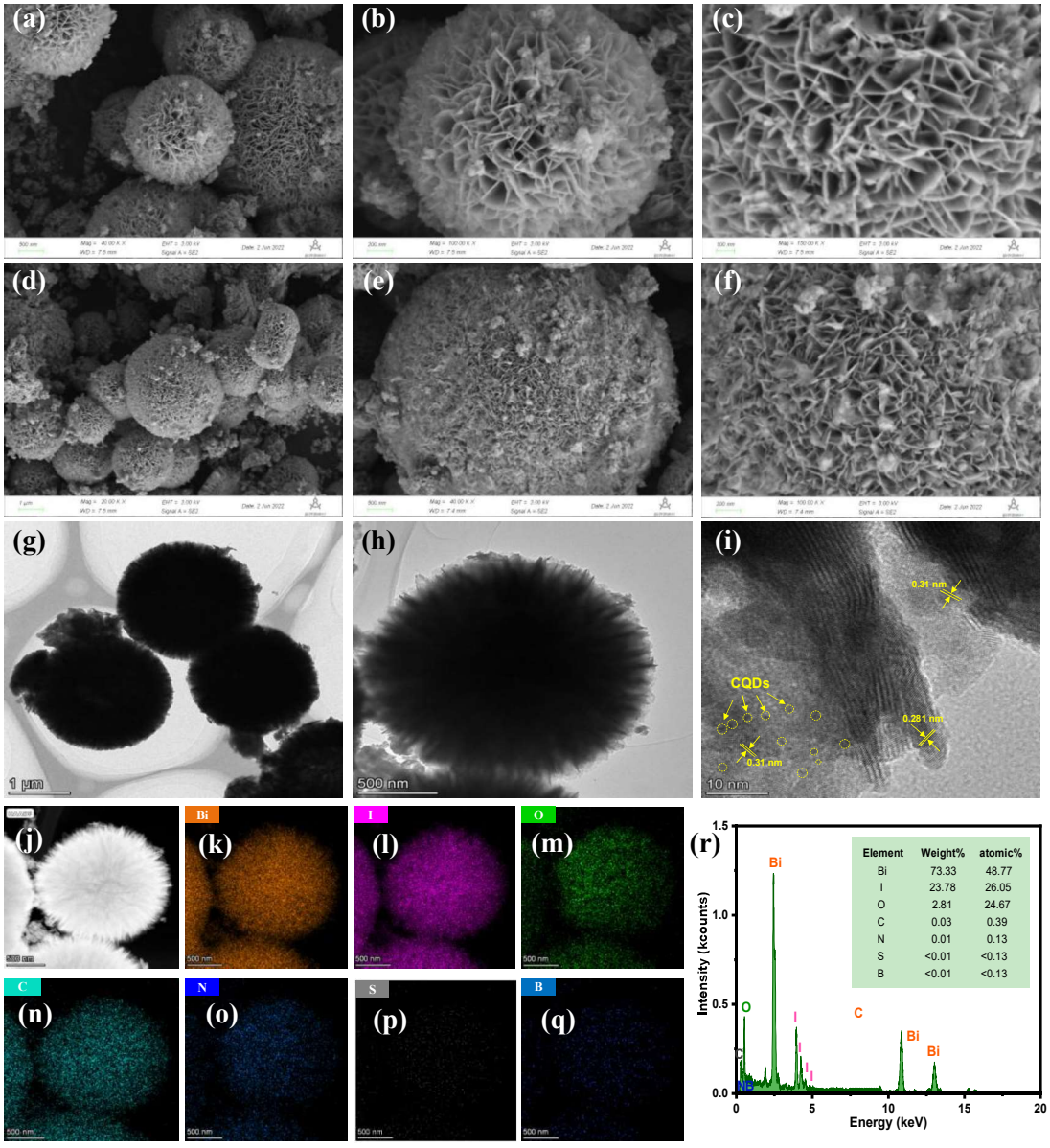

Fig. 2. SEM images of (a-c) pure $Bi_7O_9I_3$, (d-f) CQDs/$Bi_7O_9I_3$-3 composite. (g-i) TEM, HR-TEM images, (j-q) the elemental mapping elements and (r) EDS spectra of the CQDs/$Bi_7O_9I_3$-3 composite.

The chemical compositions and valence states of the as-prepared photocatalysts are further studied by XPS. **Fig. 3**a displays the survey spectra containing C 1s, O 1s, N 1s, S 2p, B 1s for CQDs, and Bi 4f, I 3d, O 1s for the pure $Bi_7O_9I_3$-3. The CQDs/$Bi_7O_9I_3$-3 composite contains most of the above elements and matches well with the elemental mapping and EDS results. In **Fig. 3**b, the Bi 4f spectra show that the two obvious peaks are located at 164.1 eV (Bi $4f_{5/2}$) and 158.88 eV (Bi $4f_{7/2}$) in $Bi_7O_9I_3$-3 and CQDs/$Bi_7O_9I_3$-3 [18]. The I 3d spectra in **Fig.3**c display two characteristic peaks at 630.1 eV (I $3d_{3/2}$) and 618.8 eV (I $3d_{5/2}$) in $Bi_7O_9I_3$ and CQDs/$Bi_7O_9I_3$-3 composite, suggesting that the valence of iodine in $Bi_7O_9I_3$ is −1 [10, 20]. The O 1s spectra in **Fig. 3**d are fitted into two peaks at 535.6 eV (C-O) and 531.6 eV (C=O) for CQDs, and at 531.1 (C=O), 529.5 eV (Bi-O) for $Bi_7O_9I_3$-3 and CQDs/$Bi_7O_9I_3$-3 [25, 26]. The C 1s spectra of CQDs and CQDs/$Bi_7O_9I_3$-3 in **Fig. 3**e can be divided into three peaks at 288.6, 286.5, and 284.8, eV, which belong to C=O, C-O/C-N and C-C/C=C, respectively [9, 27]. The N 1s spectra of CQDs and CQDs/$Bi_7O_9I_3$-3 in **Fig. 3**f mainly show the peak of N-H at 400.0 eV [28]. The B1s and S 2p of CQDs can be detected significantly (**Fig S2**a, b), whereas not detected in CQDs/$Bi_7O_9I_3$-3 composite probably due to the tiny content of B and S elements (far less than 3%).

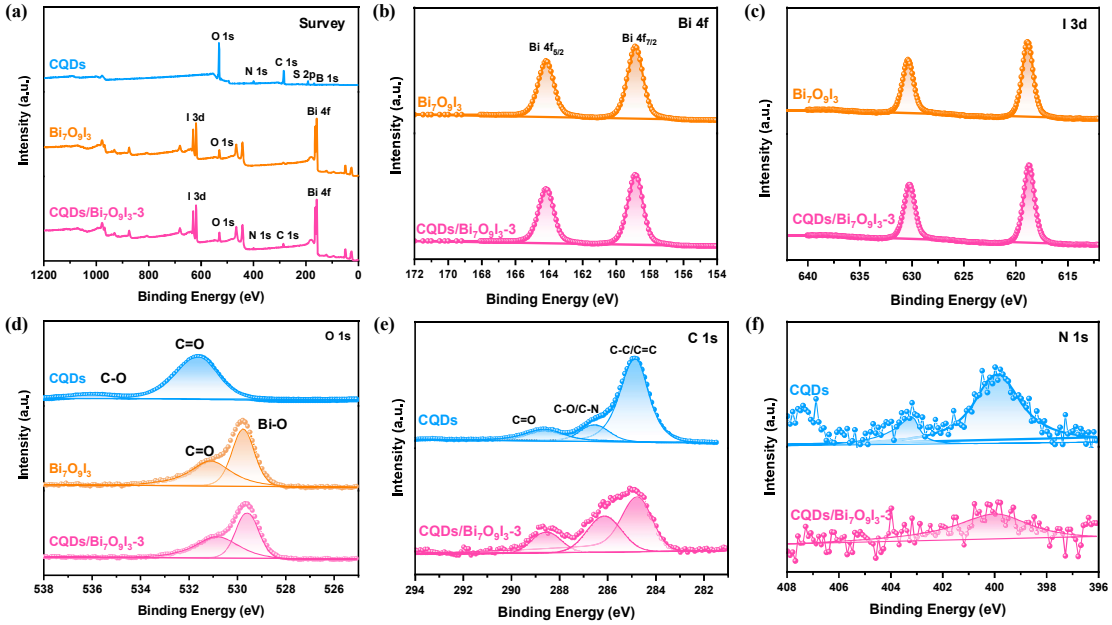

Fig. 3. (a) XPS survey spectra, high-resolution XPS spectra of (b) Bi 4f, (c) I 3d, (d) O 1s, (e) C1s, and (f) N 1s of CQDs, $Bi_7O_9I_3$, and CQDs/$Bi_7O_9I_3$-3 composite.

3.2 Optical and photoelectrochemical properties

The optical performance of the as-synthesized photocatalysts is explored by UV-vis DRS characterization. **Fig. 4**a shows that CQDs have several peaks at 215, 233, and 292 nm corresponding to π-π* transition of sp^2 conjugated structures, and 368 nm ascribed to n-π* transitions of heteroatom doping defects with a UV absorption edge of ~400 nm [29]. The $Bi_7O_9I_3$, and CQDs/$Bi_7O_9I_3$ composites present a close absorption edge of ~625 nm, implying a strong light absorption in UV and Vis regions. The CQDs/$Bi_7O_9I_3$-3 composite displays stronger absorption region at 200~450 nm probably due to the optimal adding ratio of CQDs. It demonstrates that the harvest capacity of $Bi_7O_9I_3$ is strengthened by the incorporation of CQDs, thus the availability of UV light is effectively extended. The energy bandgaps (E_g) of photocatalysts are calculated by **Eq. 1** [30]:

$$\alpha h\nu = A(h\nu - E_g)^{n/2} \quad (2)$$

Where α, hν, and A are absorption coefficients, photon energy and constant, respectively. Both CQDs and CQDs/$Bi_7O_9I_3$ composite are indirect bandgap semiconductors (n=4). The E_g of CQDs, $Bi_7O_9I_3$, CQDs/$Bi_7O_9I_3$-1, CQDs/$Bi_7O_9I_3$-3, and CQDs/$Bi_7O_9I_3$-5 are determined to be 3.43, 1.67, 1.75, 1.77, and 1.84 eV, indicating a slightly blue-shift of E_g with the incorporated of CQDs.

The PL spectra are conducted to explicate the separation efficiency of photo-generated electron-holes. The PL spectra peak of CQDs is located at 420 nm with strong intensity (**Fig S2**). It is well known that the stronger PL intensity means the rapid recombination of photo-generated electron-holes [31, 32]. As seen in **Fig. 4**b, the PL emissions peaks appear at 475 nm with a slight blue shift as the CQDs content increases, which may be due to a minor widening of Eg. The PL intensity of the photocatalysts is in the order of $Bi_7O_9I_3$ > CQDs/$Bi_7O_9I_3$-1 > CQDs/$Bi_7O_9I_3$-5 > CQDs/$Bi_7O_9I_3$-3, signifying that CQDs/$Bi_7O_9I_3$ with heterojunction structure would significantly inhibit the recombination of electron-hole pairs. The transient photocurrent response is also performed to verify the electron transfer and separation efficiency of the as-synthesized photocatalysts. In **Fig. 4**c, the pure $Bi_7O_9I_3$ presents a lower photocurrent density with four on-off irradiation cycles, indicating fast recombination of photo-generated electron-holes [33, 34]. As expected, the CQDs/ $Bi_7O_9I_3$-3 presents a remarkable improvement in photoresponse performance after the incorporation of CQDs, inferring fast electron transfer and efficient separation of electron-hole pairs. Meanwhile, the EIS analysis in **Fig. 4**d illustrates that the CQDs/$Bi_7O_9I_3$-3 possesses the smallest Nyquist circle in the high-frequency region in comparison with the other photocatalysts, suggesting the minimum charge transfer resistance [35]. It could be concluded that the formation of a tightly connected interface between CQDs

and $Bi_7O_9I_3$ accelerates the charge migration, thus promoting electron-hole pair separation.

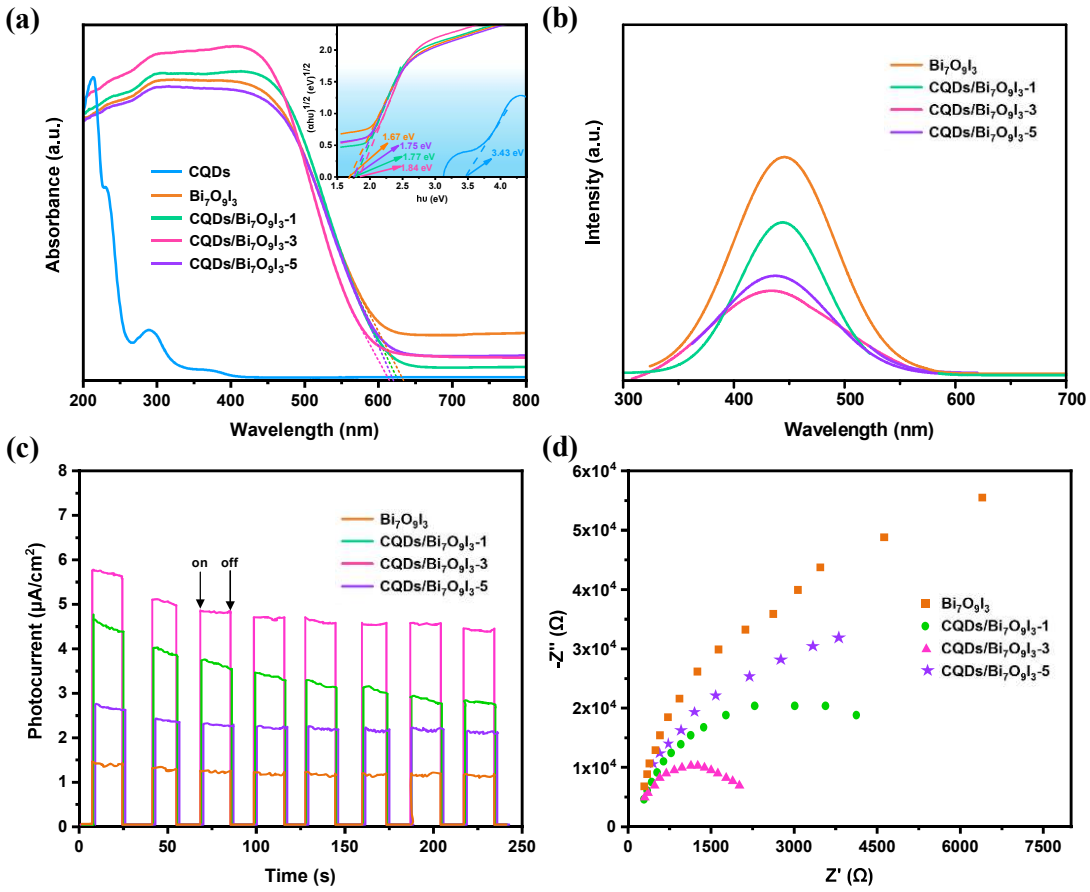

Fig. 4. (a) UV–vis DRS spectra (inset: energy bandgaps), (b) PL spectra, (c) Transient photocurrent response, and (d) EIS of CQDs, $Bi_7O_9I_3$, and CQDs/$Bi_7O_9I_3$ composites.

3.3 Photocatalytic performance

The photocatalytic performance of the prepared photocatalysts is evaluated by TC degradation under 300W Xe lamp irradiation (**Fig. 5**a). The adsorption-desorption equilibrium is attained between the photocatalysts and contaminant after constant stirring for 30 min in the darkness. The blank experiment manifests that TC can be hardly degraded without photocatalysts. The CQDs and pure $Bi_7O_9I_3$ exhibit limited degradation efficiency of 16.0%, and 70.9% after irradiation for 50 min, which could be in the reason of intensive photon scattering and rapid charge recombination. After the incorporation of CQDs, 98.2%, 100%, and 95.0% of TC can be removed by CQDs/$Bi_7O_9I_3$-1, CQDs/$Bi_7O_9I_3$-3, and CQDs/$Bi_7O_9I_3$-5 under the same conditions, respectively. Notably, the photocatalytic performance of the previously reported CQDs-based photocatalysts for TC degradation is listed in **Table S1**. The CQDs/$Bi_7O_9I_3$-3 composite in this work possesses the highest photocatalytic activity, which enables the rapidly degrade all of the contaminants within only 45 min. It could be in the reason

of enhanced UV light absorption and improved separation efficiency of electron-hole pairs by the incorporation of CQDs, which is validated by UV–vis DRS and PL spectra, respectively. Importantly, it is commercially valuable and competitive in terms of CQDs' low-cost and green raw material applied to environmental purification. Nevertheless, the excessive accumulation of CQD on the surface of CQDs/$Bi_7O_9I_3$-5 composite would inevitably hinder the light absorption and active sites, with consequently lower lowering the degradation efficiency [36-38]. Additionally, the photocatalytic degradation kinetics for CQDs, $Bi_7O_9I_3$ and CQDs/$Bi_7O_9I_3$ composites (**Fig. 5**b) are fitted with the pseudo-first-order kinetic model [18, 39, 40]:

$$-ln(C/C_0) = kt \quad (3)$$

Where k is the pseudo-first-order kinetic reaction kinetic values (min^{-1}). In agreement with the photocatalytic degradation curves, the k value of 0.08133 min^{-1} for TC degradation over CQDs/$Bi_7O_9I_3$-3 is about 31.00, 4.74, 1.44 and 2.04 times higher than that of CQDs, $Bi_7O_9I_3$, CQDs/$Bi_7O_9I_3$-1, and CQDs/$Bi_7O_9I_3$-5, respectively. These results imply that the appropriate modification by CQDs could promote the highly efficient synergistic effect of CQDs with $Bi_7O_9I_3$.

The recycling experiments are performed for the assessment of the recyclability and stability of the CQDs/$Bi_7O_9I_3$-3 composite. After five cycles, the degradation efficiency of TC for CQDs/$Bi_7O_9I_3$-3 maintains at 80%, while that for $Bi_7O_9I_3$-3 drops sharply to 30% (**Fig. 5**c). Additionally, XRD patterns of the CQDs/$Bi_7O_9I_3$-3 composite before and after five recycle experiments are measured in **Fig. 5**d. In comparison, there are no emerging peaks and significant shift appeared in the two XRD patterns, suggesting the invariant crystal structure of the reused CQDs/$Bi_7O_9I_3$-3. These results reveal the superior recyclability and stability of the as-synthesized photocatalyst.

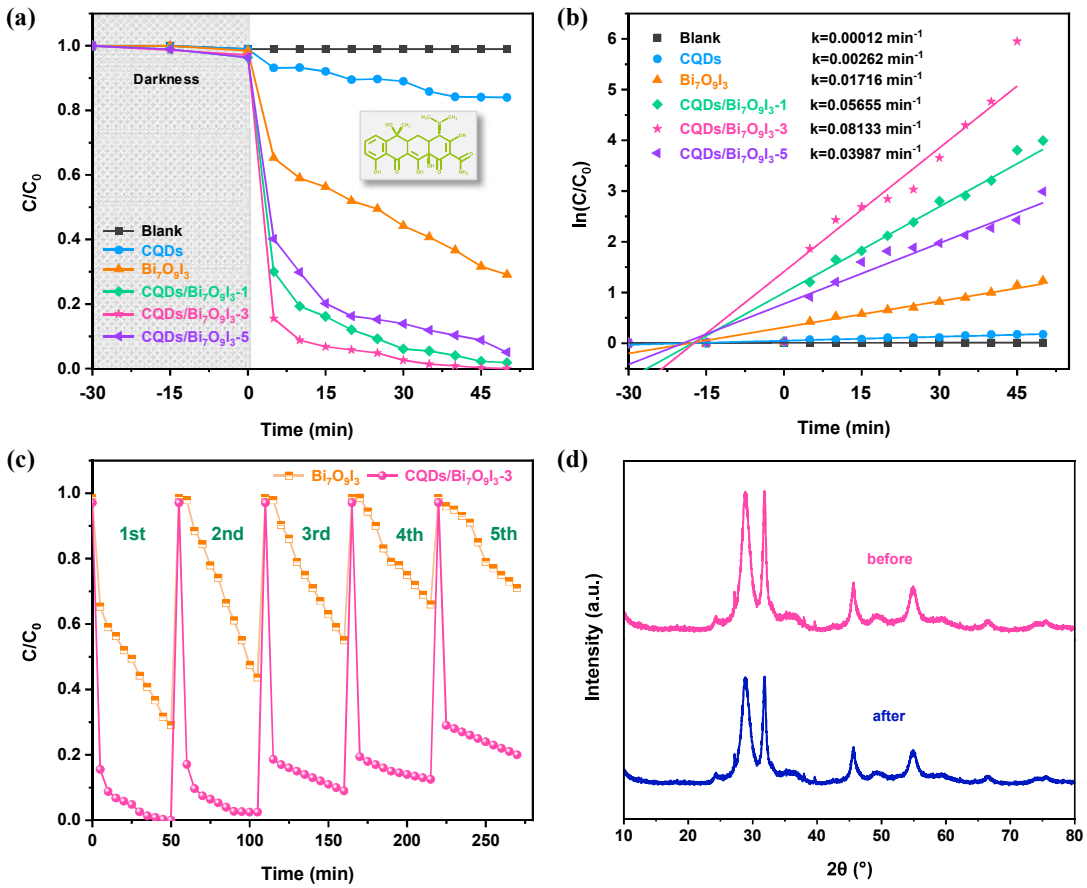

Fig. 5. (a) Photocatalytic degradation efficiency, (b) First-order kinetics for CQDs, $Bi_7O_9I_3$, and CQDs/$Bi_7O_9I_3$ composites, (c) Recycle experiments of TC degradation for $Bi_7O_9I_3$, and CQDs/$Bi_7O_9I_3$ composites, and (d) XRD patterns of initial and reused CQDs/$Bi_7O_9I_3$-3 composite.

3.4 Photocatalytic mechanism

The trapping experiments were employed to identify the predominant reactive species for TC degradation over CQDs/$Bi_7O_9I_3$-3 composite, and IPA, 1, 4-BQ and EDTA-2Na were selected as the scavengers of •OH, $•O^{2-}$ and h^+, respectively [41-43]. In **Fig. 6**a, the photocatalytic degradation efficiency of TC by CQDs/$Bi_7O_9I_3$-3 dramatically decreased to 43.8% and 23.1% in the presence of 1, 4-BQ and EDTA-2Na, as compared to 94.8% in the presence of IPA. The effects of free radicals on kinetic rate constants of TC degradation by CQDs/$Bi_7O_9I_3$-3 are in the order of h^+ (0.00352) > $•O^{2-}$ (0.00783) > •OH (0.06048) (**Fig. 6**b). These results manifest that $•O^{2-}$ and h^+ are the crucial reactive species to dominate the photocatalytic activity, while •OH exerts a slight effect on TC degradation by CQDs/$Bi_7O_9I_3$-3. To further determine the photocatalytic mechanism, the EPR measurements are carried out with a free radical scavenger (DMPO). As illustrated in **Fig. 6**c, there is no EPR signal for DMPO-

•OH of CQDs under 300W Xe lamp irradiation, and the weak quartet peaks for DMPO-•OH are obtained in the photocatalytic system of $Bi_7O_9I_3$ and CQDs/$Bi_7O_9I_3$-3. According to **Fig. 6**d, the apparent signals of DMPO-•O^{2-} with the intensity of 1:1:1:1 are detected in CQDs and CQDs/$Bi_7O_9I_3$-3 photocatalysts under 300W Xe lamp irradiation [44], while that in $Bi_7O_9I_3$ is not clearly identified. These results confirm the incorporation of CQDs contributes to the formation of •O^{2-} radicals in the photocatalytic system.

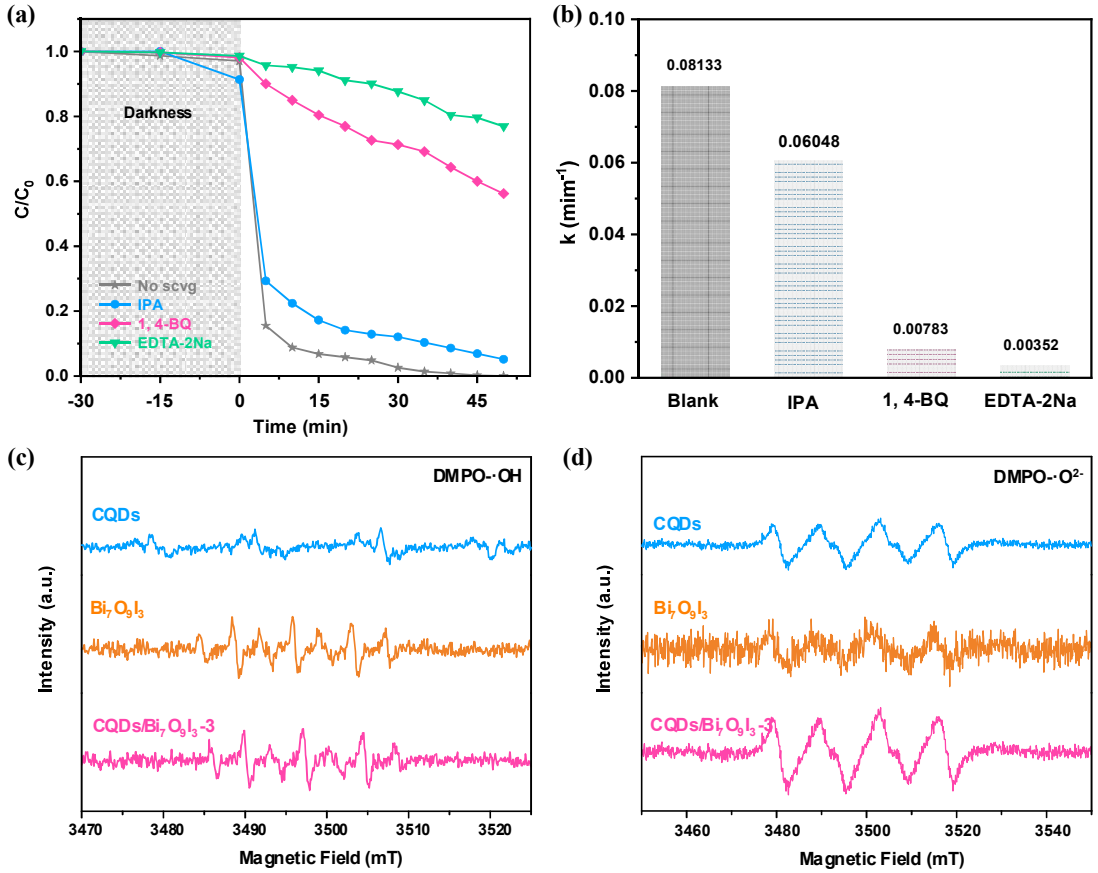

Fig. 6. (a) Photocatalytic degradation efficiency and (b) kinetic rate constants of TC degradation in the existence of three scavengers for CQDs/$Bi_7O_9I_3$-3 composite, and EPR spectra of (c) DMPO-•OH, and (d) DMPO-•O^{2-} of CQDs/$Bi_7O_9I_3$-3 composite under 300W Xe lamp irradiation.

According to the above analysis, the photocatalytic mechanism of the CQDs/$Bi_7O_9I_3$-3 composite for TC degradation is proposed in **Fig. 7**. Upon simulated sunlight irradiation of CQDs/$Bi_7O_9I_3$-3, $Bi_7O_9I_3$ is excited to generate electrons on the conduction band (CB) and holes on the valence band (VB), respectively [20]. Generally, most of the photo-generated electrons and holes are rapidly recombined rather than contributing to the photocatalytic reaction probably due to the too narrow E_g (1.77 eV) of $Bi_7O_9I_3$ [15, 45]. However, CQDs act as an excellent electron reservoir due to their outstanding conductivity of conjugated π structure, and could easily collect the electrons from CB of $Bi_7O_9I_3$. The electron transfer rate is significantly

accelerated by CQDs and the recombination of electron-hole pairs of $Bi_7O_9I_3$ is effectively inhibited [16, 46]. The established inner electric field on the tightly contacted interface of CQDs/$Bi_7O_9I_3$-3 greatly promotes the rate of photocatalytic TC degradation. Subsequently, the accumulated electrons attached to the surface of CQDs reduce the dissolved O_2 to yield $\bullet O^{2-}$ [6, 47, 48], which is confirmed to be the key radical in the photocatalytic reaction of CQDs/$Bi_7O_9I_3$-3. The holes remaining on the VB of $Bi_7O_9I_3$ would partly directly oxidize TC or react with H_2O/OH^- to produce •OH [49, 50]. The TC molecules can be attacked by these $\bullet O^{2-}$ and h^+ radicals, and ultimately decomposed into the intermediates or CO_2 and H_2O [51, 52]. Noteworthily, the abundance of different heteroatom (N, S and B) surface defect sites on the surface of CQDs facilitates the activation of O_2 molecular [15]. It reveals that the incorporation of CQDs not only enhances the sunlight harvesting ability but also improves the photocatalytic performance of CQDs/$Bi_7O_9I_3$-3 though enhancing the separation of electron-hole pairs and providing more reactive species.

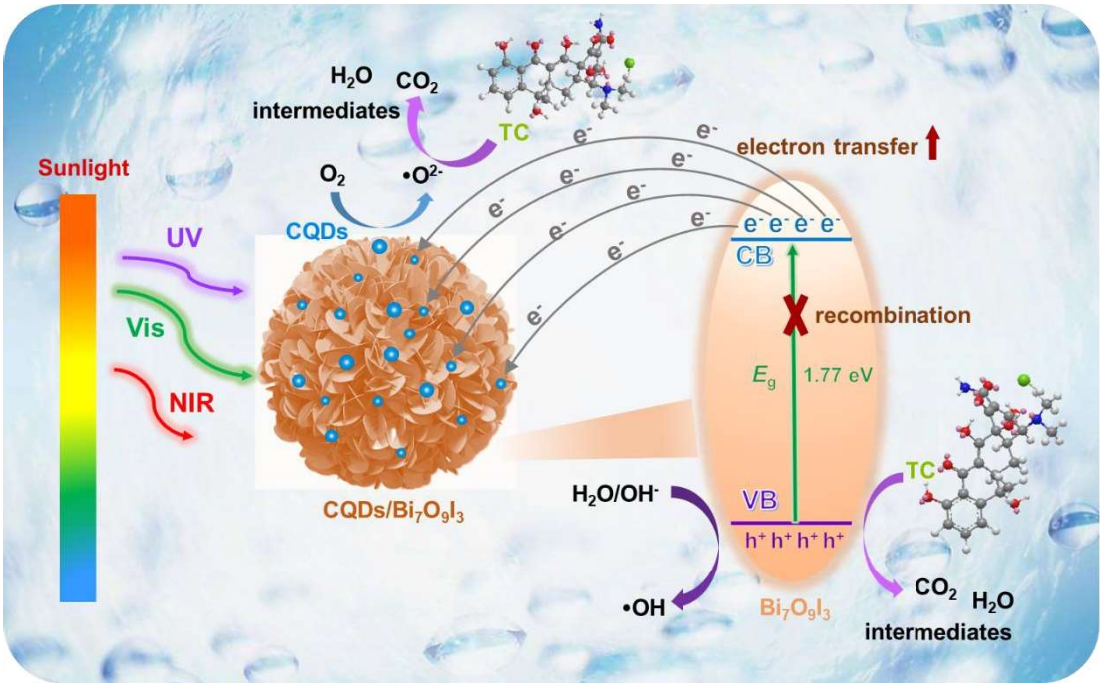

Fig. 7. Illustration of the photocatalytic mechanism of TC degradation by CQDs/$Bi_7O_9I_3$-3 composite.

4. Conclusions

The photocatalyst composites of $Bi_7O_9I_3$ decorated by lignin-derived CQDs were fabricated via a simple hydrothermal process. The CQDs were embedded on the surface of the $Bi_7O_9I_3$ nanosheet. The CQDs/$Bi_7O_9I_3$ composites had enhanced photocatalytic performance, recyclability and stability for TC degradation under Xe lamp irradiation compared to pure

$Bi_7O_9I_3$. The optimum CQDs/$Bi_7O_9I_3$-3 exhibited superior photocatalytic efficiency with nearly 100% removal of TC (10 mg/L) in 45 min and 0.08133 min^{-1} degradation rate, which was 4.74 times higher than that of pure $Bi_7O_9I_3$. The $\bullet O^{2-}$ and h^+ radicals identified by EPR and free radical trapping experiments were estimated as the key reactive species for TC degradation. The roles of CQDs in photocatalytic performance enhancement can be explained from the following aspects: (i) CQDs acted as a photosensitizer and photocenter for enhancing the sunlight harvesting ability of CQDs/$Bi_7O_9I_3$ composite; (ii) CQDs worked as an electron reservoir and reduce the dissolved O_2 to yield $\bullet O^{2-}$ radicals, thereby accelerating the charge migration and inhibiting the recombination of electron-hole pairs; (iii) The abundance of defects on the surface of CQDs extremely facilitates the activation of O_2 molecular, promoting the photocatalytic activity of CQDs/$Bi_7O_9I_3$ composite. This work has inspired the design and fabrication of more high-performance photocatalysts decorated by biomass-derived CQDs for contaminant water treatment.

Declaration of Competing Interest

The authors declare that they have no known competing financial interests or personal relationships that could have appeared to influence the work reported in this paper.

Acknowledgements

The authors gratefully acknowledge the financial support from the National Natural Science Foundation of China (grant numbers. 51676047 and 51861145102) and the Key Research & Development Program of Jiangsu Province (grant number: BE2020114). The authors also acknowledge the funding support from the Scientific Research Foundation of Graduate School of Southeast University, China (YBPY2109) and the Postgraduate Research & Practice Innovation Program of Jiangsu Province from the Education Department of Jiangsu (KYCX21_0094).

References

[1] Shen, S., Wang, H., Fu, J. A nanoporous Three-dimensional graphene aerogel doped with a carbon quantum Dot-TiO2 composite that exhibits superior activity for the catalytic photodegradation of organic pollutants. Applied Surface Science. **2021**, 569.

[2] Chen, Q., Chen, L., Qi, J., Tong, Y., Lv, Y., Xu, C., Ni, J., Liu, W. Photocatalytic degradation of amoxicillin by carbon quantum dots modified K2Ti6O13 nanotubes: Effect of light wavelength. Chinese Chemical Letters. **2019**, 30, 1214-1218.

[3] Wang, F., Wang, Y., Feng, Y., Zeng, Y., Xie, Z., Zhang, Q., Su, Y., Chen, P., Liu, Y., Yao, K., Lv, W., Liu, G. Novel ternary photocatalyst of single atom-dispersed silver and carbon

quantum dots co-loaded with ultrathin g-C3N4 for broad spectrum photocatalytic degradation of naproxen. Applied Catalysis B-Environmental. **2018**, 221, 510-520.
[4] Zhang, Q., Xu, W., Han, C., Wang, X., Wang, Y., Li, Z., Wu, W., Wu, M. Graphene structure boosts electron transfer of dual-metal doped carbon dots in photooxidation. Carbon. **2018**, 126, 128-134.
[5] Wang, Q., Wang, G., Liang, X., Dong, X., Zhang, X. Supporting carbon quantum dots on NH2-MIL-125 for enhanced photocatalytic degradation of organic pollutants under a broad spectrum irradiation. Applied Surface Science. **2019**, 467-468, 320-327.
[6] Jia, J., Jiang, C., Zhang, X., Li, P., Xiong, J., Zhang, Z., Wu, T., Wang, Y. Urea-modified carbon quantum dots as electron mediator decorated g-C3N4/WO3 with enhanced visible-light photocatalytic activity and mechanism insight. Applied Surface Science. **2019**, 495.
[7] Yue, X., Miao, X., Ji, Z., Shen, X., Zhou, H., Kong, L., Zhu, G., Li, X., Ali Shah, S. Nitrogen-doped carbon dots modified dibismuth tetraoxide microrods: A direct Z-scheme photocatalyst with excellent visible-light photocatalytic performance. J Colloid Interface Sci. **2018**, 531, 473-482.
[8] Zhu, Z., Li, X., Luo, M., Chen, M., Chen, W., Yang, P., Zhou, X. Synthesis of carbon dots with high photocatalytic reactivity by tailoring heteroatom doping. J Colloid Interface Sci. **2021**, 605, 330-341.
[9] Xiong, S., Bao, S., Wang, W., Hao, J., Mao, Y., Liu, P., Huang, Y., Duan, Z., Lv, Y., Ouyang, D. Surface oxygen vacancy and graphene quantum dots co-modified Bi2WO6 toward highly efficient photocatalytic reduction of CO2. Applied Catalysis B: Environmental. **2022**, 305.
[10] Lai, J., Jiang, X., Zhao, M., Cui, S., Yang, J., Li, Y. Thickness-dependent layered BiOIO3 modified with carbon quantum dots for photodegradation of bisphenol A: Mechanism, pathways and DFT calculation. Applied Catalysis B: Environmental. **2021**, 298.
[11] Zhang, M., Lai, C., Li, B., Huang, D., Zeng, G., Xu, P., Qin, L., Liu, S., Liu, X., Yi, H., Li, M., Chu, C., Chen, Z. Rational design 2D/2D BiOBr/CDs/g-C3N4 Z-scheme heterojunction photocatalyst with carbon dots as solid-state electron mediators for enhanced visible and NIR photocatalytic activity: Kinetics, intermediates, and mechanism insight. Journal of Catalysis. **2019**, 369, 469-481.
[12] Wang, J., Tang, L., Zeng, G., Deng, Y., Dong, H., Liu, Y., Wang, L., Peng, B., Zhang, C., Chen, F. OD/2D interface engineering of carbon quantum dots modified Bi2WO6 ultrathin nanosheets with enhanced photoactivity for full spectrum light utilization and mechanism insight. Applied Catalysis B-Environmental. **2018**, 222, 115-123.
[13] Zhu, L., Shen, D., Wu, C., Gu, S. State-of-the-Art on the Preparation, Modification, and Application of Biomass-Derived Carbon Quantum Dots. Industrial & Engineering Chemistry Research. **2020**, 59, 22017-22039.
[14] Wang, Z., Cheng, Q., Wang, X., Li, J., Li, W., Li, Y., Zhang, G. Carbon dots modified bismuth antimonate for broad spectrum photocatalytic degradation of organic pollutants: Boosted charge separation, DFT calculations and mechanism unveiling. Chemical Engineering Journal. **2021**, 418.
[15] Zhang, J., Yuan, X., Jiang, L., Wu, Z., Chen, X., Wang, H., Wang, H., Zeng, G. Highly efficient photocatalysis toward tetracycline of nitrogen doped carbon quantum dots sensitized bismuth tungstate based on interfacial charge transfer. J Colloid Interface Sci.

2018, 511, 296-306.
[16] Zhang, J., Si, M., Jiang, L., Yuan, X., Yu, H., Wu, Z., Li, Y., Guo, J. Core-shell Ag@nitrogen-doped carbon quantum dots modified BiVO4 nanosheets with enhanced photocatalytic performance under Vis-NIR light: Synergism of molecular oxygen activation and surface plasmon resonance. Chemical Engineering Journal. **2021**, 410.
[17] Zhou, Q., Huang, W., Xu, C., Liu, X., Yang, K., Li, D., Hou, Y., Dionysiou, D.D. Novel hierarchical carbon quantum dots-decorated BiOCl nanosheet/carbonized eggshell membrane composites for improved removal of organic contaminants from water via synergistic adsorption and photocatalysis. Chemical Engineering Journal. **2021**, 420.
[18] Liang, L., Gao, S., Zhu, J., Wang, L., Xiong, Y., Xia, X., Yang, L. The enhanced photocatalytic performance toward carbamazepine by nitrogen-doped carbon dots decorated on BiOBr/CeO2: Mechanism insight and degradation pathways. Chemical Engineering Journal. **2020**, 391.
[19] Zhu, L., Shen, D., Wang, Q., Luo, K.H. Green Synthesis of Tunable Fluorescent Carbon Quantum Dots from Lignin and Their Application in Anti-Counterfeit Printing. ACS Applied Materials & Interfaces. **2021**.
[20] Yuan, Y., Guo, R.T., Hong, L.F., Lin, Z.D., Ji, X.Y., Pan, W.G. Fabrication of a dual S-scheme Bi7O9I3/g-C3N4/Bi3O4Cl heterojunction with enhanced visible-light-driven performance for phenol degradation. Chemosphere. **2022**, 287, 132241.
[21] Zhu, L., Shen, D., Liu, Q., Wu, C., Gu, S. Sustainable synthesis of bright green fluorescent carbon quantum dots from lignin for highly sensitive detection of Fe^{3+} ions. Applied Surface Science. **2021**, 565.
[22] Zhu, L., Shen, D., Hong Luo, K. Triple-emission nitrogen and boron co-doped carbon quantum dots from lignin: Highly fluorescent sensing platform for detection of hexavalent chromium ions. J Colloid Interface Sci. **2022**, 617, 557-567.
[23] Xie, R., Zhang, L., Xu, H., Zhong, Y., Sui, X., Mao, Z. Construction of up-converting fluorescent carbon quantum dots/Bi20TiO32 composites with enhanced photocatalytic properties under visible light. Chemical Engineering Journal. **2017**, 310, 79-90.
[24] Le, S., Li, W., Wang, Y., Jiang, X., Yang, X., Wang, X. Carbon dots sensitized 2D-2D heterojunction of BiVO4/Bi3TaO7 for visible light photocatalytic removal towards the broad-spectrum antibiotics. Journal of Hazardous Materials. **2019**, 376, 1-11.
[25] Kim, S.-R., Jo, W.-K. Boosted photocatalytic decomposition of nocuous organic gases over tricomposites of N-doped carbon quantum dots, ZnFe2O4, and BiOBr with different junctions. Journal of Hazardous Materials. **2019**, 380.
[26] Cui, Y., Wang, T., Liu, J., Hu, L., Nie, Q., Tan, Z., Yu, H. Enhanced solar photocatalytic degradation of nitric oxide using graphene quantum dots/bismuth tungstate composite catalysts. Chemical Engineering Journal. **2021**, 420.
[27] Mahmood, A., Shi, G., Wang, Z., Rao, Z., Xiao, W., Xie, X., Sun, J. Carbon quantum dots-TiO2 nanocomposite as an efficient photocatalyst for the photodegradation of aromatic ring-containing mixed VOCs: An experimental and DFT studies of adsorption and electronic structure of the interface. J Hazard Mater. **2021**, 401, 123402.
[28] Li, Q., Wang, S., Sun, Z., Tang, Q., Liu, Y., Wang, L., Wang, H., Wu, Z. Enhanced CH4 selectivity in CO2 photocatalytic reduction over carbon quantum dots decorated and oxygen doping g-C3N4. Nano Research. **2019**, 12, 2749-2759.

[29] Liu, Y., Yang, H., Ma, C., Luo, S., Xu, M., Wu, Z., Li, W., Liu, S. Luminescent Transparent Wood Based on Lignin-Derived Carbon Dots as a Building Material for Dual-Channel, Real-Time, and Visual Detection of Formaldehyde Gas. ACS Appl Mater Interfaces. **2020**, 12, 36628-36638.
[30] Zhu, M., Han, M., Zhu, C., Hu, L., Huang, H., Liu, Y., Kang, Z. Strong coupling effect at the interface of cobalt phosphate-carbon dots boost photocatalytic water splitting. J Colloid Interface Sci. **2018**, 530, 256-263.
[31] Wang, W., Zeng, Z., Zeng, G., Zhang, C., Xiao, R., Zhou, C., Xiong, W., Yang, Y., Lei, L., Liu, Y., Huang, D., Cheng, M., Yang, Y., Fu, Y., Luo, H., Zhou, Y. Sulfur doped carbon quantum dots loaded hollow tubular g-C3N4 as novel photocatalyst for destruction of Escherichia coli and tetracycline degradation under visible light. Chemical Engineering Journal. **2019**, 378.
[32] Si, Q., Guo, W., Wang, H., Liu, B., Zheng, S., Zhao, Q., Luo, H., Ren, N., Yu, T. Difunctional carbon quantum dots/g-C3N4 with in-plane electron buffer for intense tetracycline degradation under visible light: Tight adsorption and smooth electron transfer. Applied Catalysis B: Environmental. **2021**, 299.
[33] Ming, H., Wei, D., Yang, Y., Chen, B., Yang, C., Zhang, J., Hou, Y. Photocatalytic activation of peroxymonosulfate by carbon quantum dots functionalized carbon nitride for efficient degradation of bisphenol A under visible-light irradiation. Chemical Engineering Journal. **2021**, 424.
[34] Wang, F., Wu, Y., Wang, Y., Li, J., Jin, X., Zhang, Q., Li, R., Yan, S., Liu, H., Feng, Y., Liu, G., Lv, W. Construction of novel Z-scheme nitrogen-doped carbon dots/{001} TiO2 nanosheet photocatalysts for broad-spectrum-driven diclofenac degradation: Mechanism insight, products and effects of natural water matrices. Chemical Engineering Journal. **2019**, 356, 857-868.
[35] Han, X., Chang, Q., Li, N., Wang, H., Yang, J., Hu, S. In-situ incorporation of carbon dots into mesoporous nickel boride for regulating photocatalytic activities. Carbon. **2018**, 137, 484-492.
[36] Yuan, A., Lei, H., Xi, F., Liu, J., Qin, L., Chen, Z., Dong, X. Graphene quantum dots decorated graphitic carbon nitride nanorods for photocatalytic removal of antibiotics. Journal of Colloid and Interface Science. **2019**, 548, 56-65.
[37] Liu, J., Xu, H., Xu, Y., Song, Y., Lian, J., Zhao, Y., Wang, L., Huang, L., Ji, H., Li, H. Graphene quantum dots modified mesoporous graphite carbon nitride with significant enhancement of photocatalytic activity. Applied Catalysis B-Environmental. **2017**, 207, 429-437.
[38] Qu, Y., Xu, X., Huang, R., Qi, W., Su, R., He, Z. Enhanced photocatalytic degradation of antibiotics in water over functionalized N,S-doped carbon quantum dots embedded ZnO nanoflowers under sunlight irradiation. Chemical Engineering Journal. **2020**, 382.
[39] Ebrahimi, M., Samadi, M., Yousefzadeh, S., Soltani, M., Rahimi, A., Chou, T.-c., Chen, L. C., Chen, K. H., Moshfegh, A.Z. Improved Solar-Driven Photocatalytic Activity of Hybrid Graphene Quantum Dots/ZnO Nanowires: A Direct Z-Scheme Mechanism. ACS Sustainable Chemistry & Engineering. **2016**, 5, 367-375.
[40] Pan, D., Jiao, J., Li, Z., Guo, Y., Feng, C., Liu, Y., Wang, L., Wu, M. Efficient Separation of Electron–Hole Pairs in Graphene Quantum Dots by TiO2 Heterojunctions for Dye

Degradation. ACS Sustainable Chemistry & Engineering. **2015**, 3, 2405-2413.
[41] Cai, T., Chang, Q., Liu, B., Hao, C., Yang, J., Hu, S. Triggering photocatalytic activity of carbon dot-based nanocomposites by a self-supplying peroxide. Journal of Materials Chemistry A. **2021**, 9, 8991-8997.
[42] Cai, T., Chang, Q., Liu, B., Hao, C., Yang, J., Hu, S. Triggering photocatalytic activity of carbon dot-based nanocomposites by a self-supplying peroxide dagger. Journal of Materials Chemistry A. **2021**, 9, 8991-8997.
[43] Ma, R., Wang, L., Wang, H., Liu, Z., Xing, M., Zhu, L., Meng, X., Xiao, F. S. Solid acids accelerate the photocatalytic hydrogen peroxide synthesis over a hybrid catalyst of titania nanotube with carbon dot. Applied Catalysis B: Environmental. **2019**, 244, 594-603.
[44] Wu, X., Zhao, Q., Guo, F., Xia, G., Tan, X., Lv, H., Feng, Z., Wu, W., Zheng, J., Wu, M. Porous g-C3N4 and α-FeOOH bridged by carbon dots as synergetic visible-light-driven photo-fenton catalysts for contaminated water remediation. Carbon. **2021**, 183, 628-640.
[45] Wang, F., Chen, P., Feng, Y., Xie, Z., Liu, Y., Su, Y., Zhang, Q., Wang, Y., Yao, K., Lv, W., Liu, G. Facile synthesis of N-doped carbon dots/g-C3N4 photocatalyst with enhanced visible-light photocatalytic activity for the degradation of indomethacin. Applied Catalysis B-Environmental. **2017**, 207, 103-113.
[46] Chen, R., Chen, Z., Ji, M., Chen, H., Liu, Y., Xia, J., Li, H. Enhanced reactive oxygen species activation for building carbon quantum dots modified Bi5O7I nanorod composites and optimized visible-light-response photocatalytic performance. J Colloid Interface Sci. **2018**, 532, 727-737.
[47] Hu, Y., Guan, R., Zhang, C., Zhang, K., Liu, W., Shao, X., Xue, Q., Yue, Q. Fluorescence and photocatalytic activity of metal-free nitrogen-doped carbon quantum dots with varying nitrogen contents. Applied Surface Science. **2020**, 531.
[48] Zhang, Y., Wang, L., Yang, M., Wang, J., Shi, J. Carbon quantum dots sensitized ZnSn(OH)6 for visible light-driven photocatalytic water purification. Applied Surface Science. **2019**, 466, 515-524.
[49] Nugraha, M.W., Zainal Abidin, N.H., Supandi, Sambudi, N.S. Synthesis of tungsten oxide/ amino-functionalized sugarcane bagasse derived-carbon quantum dots (WO3/N-CQDs) composites for methylene blue removal. Chemosphere. **2021**, 277, 130300.
[50] Ding, P., Di, J., Chen, X., Ji, M., Gu, K., Yin, S., Liu, G., Zhang, F., Xia, J., Li, H. S, N Codoped Graphene Quantum Dots Embedded in (BiO)2CO3: Incorporating Enzymatic-like Catalysis in Photocatalysis. ACS Sustainable Chemistry & Engineering. **2018**, 6, 10229-10240.
[51] Li, J. F., Zhong, C. Y., Huang, J. R., Chen, Y., Wang, Z., Liu, Z. Q. Carbon dots decorated three-dimensionally ordered macroporous bismuth-doped titanium dioxide with efficient charge separation for high performance photocatalysis. Journal of Colloid and Interface Science. **2019**, 553, 758-767.
[52] Ji, M., Zhang, Z., Xia, J., Di, J., Liu, Y., Chen, R., Yin, S., Zhang, S., Li, H. Enhanced photocatalytic performance of carbon quantum dots/BiOBr composite and mechanism investigation. Chinese Chemical Letters. **2018**, 29, 805-810.

Declaration of Interest Statement

Declaration of interests

☒ The authors declare that they have no known competing financial interests or personal relationships that could have appeared to influence the work reported in this paper.

☐The authors declare the following financial interests/personal relationships which may be considered as potential competing interests: